Analysis of the (N,xN') reactions by quantum molecular dynamics plus statistical decay model

Koji Niita

Advanced Science Research Center, Japan Atomic Energy Research Institute, Tokai, Ibaraki 319-11 Japan
and Research Organization for Information Science and Technology, Tokai, Ibaraki 319-11 Japan

Satoshi Chiba, Toshiki Maruyama, Tomoyuki Maruyama, Hiroshi Takada, Tokio Fukahori, Yasuaki Nakahara,
and Akira Iwamoto

Advanced Science Research Center, Japan Atomic Energy Research Institute, Tokai, Ibaraki 319-11 Japan

We propose a model based on quantum molecular dynamics (QMD) incorporated with a statistical decay model (SDM) to describe various nuclear reactions in a unified way. In this first part of the work, the basic ingredients of the model are defined and the model is applied systematically to the nucleon- (N-)induced reactions. It has been found that our model can give a remarkable agreement in the energy-angle double differential cross sections of (N,xN') type reactions for incident energies from 100 MeV to 3 GeV with a fixed parameter set. A unified description of the three major reaction mechanisms of (N,xN') reactions, i.e., compound, preequilibrium, and spallation processes, is given with our model.

I. INTRODUCTION

Nuclear reactions reveal various aspects of the hadronic many-body problem as a function of the target and projectile combination, the incident energy, and the angular momentum involved. In nucleon-induced reactions, for example, the compound process is dominant in the low energy region, while the preequilibrium and spallation processes become more likely as the incident energy increases. In heavy-ion collisions, we also have to introduce various models of different natures depending on each specific process. However, most of them are restricted to the specific energy regime or specific phenomenon and some of them have too many parameters to obtain a definite physical conclusion from the analysis.

The main purpose of the series of our work is to develop a model which can describe the various aspects of nuclear reactions in a unified way. We try to seek a model with a minimum number of parameters, a wide range of applicability, and quantitative agreement with as many observables as possible. In addition to these requests, we require the model to be so simple that one can run its computer code on workstations.

In heavy-ion physics, microscopic models, which describe reactions in terms of the dynamics of the interacting nucleons, are commonly used to extract information on the nuclear matter under extreme conditions from the final observables. The most popular models of this type are the Boltzmann-Uehling-Uhlenbeck/Vlasov-Uehling-Uhlenbeck (BUU/VUU) [1], the quantum molecular dynamics (QMD) [2], and CASCADE type models [3,4]. So far these microscopic models have shed light on several exciting topics in heavy-ion physics, e.g., multifragmentation, the flow of nuclear matter, and energetic particle production. However, the parameters of the models, such as the effective interaction and elastic and inelastic channels of the NN cross section, differ substantially from one model to another even in the same type of model. Furthermore, these models have

not been tested intensively in much simpler light-ion reactions except for an analysis of (p,xn) reactions carried out by Peilert *et al.* [5]. In their analysis, however, the lower part of the neutron energy spectrum cannot be treated, since statistical decay following the QMD process was not included. We thus start the series of our work from the analysis of the simplest type of reactions, the (N,xN') (nucleon in, nucleon out) reaction, in this paper, aiming to establish a unified model for various nuclear reactions. In subsequent works, we are planning to analyze $(N,x\pi)$, (π,xN), and heavy-ion reactions.

We restrict our subject to the reactions of nucleon-nucleus, meson-nucleus, and nucleus-nucleus collisions with energies well above the Coulomb barrier up to several GeV/nucleon, where the classical treatment of the collisions is justified in a first-order approximation. We do not deal with phenomena which are dominated by quantum effects. In this energy regime, the whole reaction process can be divided into two parts, i.e., the dynamical process and the statistical process. These two processes are well separated in their time scales. In the dynamical process, the direct reactions, non-equilibrium reactions, and dynamical formation of highly excited fragments take place during typical collision times of the order of 10^{-22} sec. After that, evaporation and fission decay, which we call the statistical process, occur in a longer time scale of the order of 10^{-21}–10^{-15} sec. We thus employ a two-step model, namely, we incorporate quantum molecular dynamics (QMD) for the dynamical process with the statistical decay model (SDM). Similar hybrid models have been used in the analysis of heavy-ion collisions [6–8].

In this paper, we define the basic ingredients of the QMD plus SDM model and discuss how these two are combined without introducing any additional parameter. We then apply this model systematically to (N,xN') reactions, and discuss which element in the model is crucial for describing these reactions and what is necessary to develop the model further. In Sec. II we describe the details of the QMD, the effective interaction, the NN elastic and inelastic cross sections, the

relativistic corrections, and the statistical decay model employed in our model. In Sec. III we compare the various double differential cross sections calculated by this model with the experimental data for proton-induced reactions with incident energies from 100 MeV up to 3 GeV. We summarize and conclude this work in Sec. IV.

II. DESCRIPTION OF THE BASIC MODEL

As we mentioned above, our basic model consists of two parts, the quantum molecular dynamics (QMD) and the statistical decay model (SDM). The reason for employing the QMD model for the description of the dynamical processes is that the QMD can calculate the fragment formation in a natural and practical way. Though the QMD method is widely used in the study of nuclear fragmentation [2], the details of the prescription differ from author to author. Aiming to establish a simple standard model, we will start from the standard type of QMD, taking into account the relativistic kinematics and the relativistic correction for the effective interaction. Additionally, we treat the resonances of the nucleon, Δ, and $N^*(1440)$, and real pions with their isospin degrees of freedom in the equation of motion. For the statistical decay process, we use a simple prescription including only the light-particle evaporation.

A. Quantum molecular dynamics

1. Basic equations and effective interaction

The QMD method is a semiclassical simulation method in which each nucleon state is represented by a Gaussian wave function of width L,

$$\phi_i(\mathbf{r}) = \frac{1}{(2\pi L)^{3/4}} \exp\left[-\frac{(\mathbf{r}-\mathbf{R}_i)^2}{4L} + \frac{i}{\hbar}\mathbf{r}\cdot\mathbf{P}_i \right], \qquad (1)$$

where $\mathbf{R}_i$ and $\mathbf{P}_i$ are the centers of position and momentum of the ith nucleon, respectively. The total wave function is assumed to be a direct product of these wave functions. Thus the one-body distribution function is obtained by the Wigner transform of the wave function,

$$f(\mathbf{r},\mathbf{p}) = \sum_i f_i(\mathbf{r},\mathbf{p}), \qquad (2)$$

$$f_i(\mathbf{r},\mathbf{p}) = 8 \exp\left[-\frac{(\mathbf{r}-\mathbf{R}_i)^2}{2L} - \frac{2L(\mathbf{p}-\mathbf{P}_i)^2}{\hbar^2} \right]. \qquad (3)$$

The time evolution of $\mathbf{R}_i$ and $\mathbf{P}_i$ is described by Newtonian equations and the stochastic two-body collision term. The Newtonian equations are derived on the basis of the time-dependent variational principle [2] as

$$\dot{\mathbf{R}}_i = \frac{\partial H}{\partial \mathbf{P}_i}, \qquad \dot{\mathbf{P}}_i = -\frac{\partial H}{\partial \mathbf{R}_i}, \qquad (4)$$

where the Hamiltonian H consists of the single-particle energy including the mass term and the energy of the two-body interaction. As for the effective interaction, we adopt the

Skyrme type, the Coulomb, and the symmetry terms in this paper. By using the Gaussian function of nucleons [Eq. (3)], we get

$$H = \sum_i E_i + \frac{1}{2}\frac{A}{\rho_0}\sum_i \langle\rho_i\rangle + \frac{1}{1+\tau}\frac{B}{\rho_0^\tau}\sum_i \langle\rho_i\rangle^\tau$$

$$+ \frac{1}{2}\sum_{i,j(\neq i)} c_i c_j \frac{e^2}{|\mathbf{R}_i-\mathbf{R}_j|} \mathrm{erf}(|\mathbf{R}_i-\mathbf{R}_j|/\sqrt{4L})$$

$$+ \frac{C_s}{2\rho_0}\sum_{i,j(\neq i)} (1-2|c_i-c_j|) \rho_{ij}, \qquad (5)$$

with

$$E_i = \sqrt{m_i^2 + \mathbf{P}_i^2} , \qquad (6)$$

where erf denotes the error function. In the above equation, c_i is 1 for protons and 0 for neutrons, while $\langle\rho_i\rangle$ is an overlap of density with other nucleons defined as

$$\langle\rho_i\rangle \equiv \sum_{j\neq i} \rho_{ij} \equiv \sum_{j\neq i} \int d\mathbf{r} \, \rho_i(\mathbf{r}) \, \rho_j(\mathbf{r})$$

$$= \sum_{j\neq i} (4\pi L)^{-3/2}\exp[-(\mathbf{R}_i-\mathbf{R}_j)^2/4L], \qquad (7)$$

with

$$\rho_i(\mathbf{r}) \equiv \int \frac{d\mathbf{p}}{(2\pi\hbar)^3} f_i(\mathbf{r},\mathbf{p})$$

$$= (2\pi L)^{-3/2}\exp[-(\mathbf{r}-\mathbf{R}_i)^2/2L]. \qquad (8)$$

In this paper we use the parameters $A = -219.4$ MeV, $B = 165.3$ MeV, and $\tau = 4/3$ which yield a compressibility of $K = 237.3$ MeV, saturation at $\rho = \rho_0 = 0.168$ fm^{-3}, and a binding energy of 16 MeV per nucleon for infinite nuclear matter. The symmetry energy parameter C_s is chosen to be 25 MeV. The width of the Gaussian L is a parameter of the QMD and fixed as $L = 2.0$ fm^2 in this paper.

2. Two-body collision term

In addition to the Newtonian equation Eq. (4), the time evolution of the system is affected by the two-body collision term. In the QMD method, the stochastic two-body collision process is introduced in a phenomenological way on the analogy of the test-particle calculation of the BUU collision term [1]. It includes the Pauli blocking factor $[1-f(\mathbf{r},\mathbf{p},t)]$, which is lacking in the cascade collision process [3,4]. We follow basically the prescription of the two-body collision term used in the BUU calculation done by Wolf et al. [9,10], and modify it to extend the energy range up to 3 GeV. We thus describe here the outline of the procedure of Refs. [9,10] and explain the extensions introduced in this paper. Further details of the collision term and the dynamics of Δ's, N^*'s, and pions discussed below can be found in Refs. [9,10].

It is assumed that two particles collide if their impact parameter defined in a covariant way is smaller than a given value $b_{\max} = \sqrt{\sigma/\pi}$ obtained from the cross section σ. The collisions are considered as an instantaneous interaction and

a collision event is specified by the two points in space-time where the collision happens. Therefore it is hard to retain the covariance, since one has to choose a common reference frame for the QMD calculations. Hence the average proper time of the collision points defined by each particle is used to determine the time step in which the collision happens. This collision prescription was checked for heavy-ion collisions from 400 MeV/nucleon to 2.1 GeV/nucleon, and it was found that the disturbance of the covariance was very small [9].

In order to treat reactions with high bombarding energies, we include in our QMD simulation the nucleons (N), deltas [$\Delta(1232)$], $N^*(1440)$'s, and pions with their isospin degree of freedom. The Δ's and N^*'s are propagated in the same interactions as the nucleons except for the symmetry term, while pions are affected only by the Coulomb interaction. The creation and absorption of these particles are treated in the collision term. In the following, we list all channels included in the collision term, where B denotes a baryon and N, more specifically, a nucleon:

1. $B_i + B_j \rightarrow B_i + B_j$,

2. $N + N \rightarrow N + \Delta$,

3. $N + \Delta \rightarrow N + N$,

4. $N + N \rightarrow N + N^*$,   (9)

5. $N + N^* \rightarrow N + N$,

6. $N + \pi \rightarrow \Delta$,

7. $N + \pi \rightarrow N^*$,

8. $\Delta + \pi \rightarrow N^*$.

The channel 8 has been added to the prescription of Wolf *et al.* [9], and is the inverse process of the additional decay channel of $N^*(1440)$'s (cf. channel 11 below).

We use the following parametrization for all baryon-baryon elastic cross sections [channel 1 in Eq. (9)],

$$\sigma = \frac{C_1}{1 + 100\sqrt{s'}} + C_2 \quad \text{(mb)}, \quad (10)$$

with

$$\sqrt{s'} = \max(0, \sqrt{s} - M_i - M_j - \text{cutoff}) \quad \text{(GeV)}, \quad (11)$$

where the cutoff is 0.02 GeV for the nucleon-nucleon channel, while it is zero for the others. This is the conventional Cugnon parametrization form [1,4]. We use this form up to $\sqrt{s'} = 0.4286$ (GeV), which corresponds to 1 GeV lab energy for the nucleon-nucleon case. Above 1 GeV, we parametrize the experimental p-p and p-n elastic cross sections [11,12] as

$$\sigma = C_3 \left[1 - \frac{2}{\pi} \tan^{-1}(1.5\sqrt{s'} - 0.8) \right] + C_4 \quad \text{(mb)}. \quad (12)$$

In order to connect Eqs. (10) and (12) smoothly, we slightly modified the parameters of Cugnon [1,4]. The actual values of the parameters C_i in the above equations are listed in Table I. The angular distribution of the elastic channels is taken from the same form as Cugnon parametrization [1,4].

TABLE I. Elastic cross section parameters.

	p-n	Others
C_1 (mb)	28.0	35.0
C_2 (mb)	27.0	20.0
C_3 (mb)	12.34	9.65
C_4 (mb)	10.0	7.0

For the production of baryonic resonances [channels 2 and 4 in Eq. (9)], we adopt the total cross section based on the parametrization of VerWest and Arndt [13], in which the pion cross sections are parametrized assuming the pions are produced through baryonic resonances. Their parametrization was performed by fitting the experimental data up to 1.5 GeV incident energy. In order to extend the energy range up to 3 GeV, we have modified the parameters in the following way. In the model of VerWest and Arndt, the cross sections are parametrized according to the initial and final total isospin i and f of the two-nucleon system [13] as

$$\sigma_{if}(s) = \frac{\pi(\hbar c)^2}{2p^2} \alpha \left(\frac{p_r}{p_0}\right)^\beta \frac{m_0^2 \Gamma^2 (q/q_0)^3}{(s^* - m_0^2)^2 + m_0^2 \Gamma^2}, \quad (13)$$

where

$$p_0^2 = \frac{1}{4} s_0 - m_N^2, \quad s_0 = (m_N + m_0)^2,$$

$$p_r^2(s) = \frac{[s - (m_N - \langle M \rangle)^2][s - (m_N + \langle M \rangle)^2]}{4s},$$

$$q^2(s^*) = \frac{[s^* - (m_N - m_\pi)^2][s^* - (m_N + m_\pi)^2]}{4s^*}, \quad (14)$$

$$s^* = \langle M \rangle^2, \quad q_0 = q(m_0^2),$$

and $\langle M \rangle$ is the mean mass of the resonance [13] obtained from a Breit-Wigner distribution with $M_0 = 1220$ MeV and, $\Gamma_0 = 120$ MeV for the Δ and $M_0 = 1430$ MeV and $\Gamma_0 = 200$ MeV for the N^*. From these cross sections, we determine the production cross section of Δ's [9] as

$$
\begin{aligned}
p + p &\rightarrow n + \Delta^{++} &:& \quad \sigma_{10} + \tfrac{1}{2}\sigma_{11}, \\
p + p &\rightarrow p + \Delta^{+} &:& \quad \tfrac{3}{2}\sigma_{11}, \\
n + p &\rightarrow p + \Delta^{0} &:& \quad \tfrac{1}{2}\sigma_{11} + \tfrac{1}{4}\sigma_{10}, \\
n + p &\rightarrow n + \Delta^{+} &:& \quad \tfrac{1}{2}\sigma_{11} + \tfrac{1}{4}\sigma_{10}, \\
n + n &\rightarrow p + \Delta^{-} &:& \quad \sigma_{10} + \tfrac{1}{2}\sigma_{11}, \\
n + n &\rightarrow n + \Delta^{0} &:& \quad \tfrac{3}{2}\sigma_{11}.
\end{aligned}
\quad (15)
$$

We have effectively included the cross section of the πd final state, parametrized as σ_{10}^d in [13], in the cross section of σ_{10}.

We assume in this paper that the cross section σ_{01} in [13] contributes only to the N^* production independently of the isospin components. Thus we rename σ_{01} as σ_{N*}, and the N^* production cross sections are given by

TABLE II. Inelastic cross section parameters.

	σ_{11}	σ_{10}	σ_{N*}
α	3.0	14.0	23.0
β	0.9	-0.3	1.5
m_0 (MeV)	1188	1245	1472
Γ (MeV)	99.02	120.0	300.0

$$
\begin{aligned}
p+p &\rightarrow p+N^{*+} &:& \quad \tfrac{3}{2}\,\sigma_{N*}, \\
n+p &\rightarrow p+N^{*0} &:& \quad \tfrac{3}{4}\,\sigma_{N*}, \\
n+p &\rightarrow n+N^{*+} &:& \quad \tfrac{3}{4}\,\sigma_{N*}, \\
n+n &\rightarrow n+N^{*0} &:& \quad \tfrac{3}{2}\,\sigma_{N*}.
\end{aligned}
\qquad (16)
$$

The new parameters in Eq. (13) are given in Table II. In order to determine these parameters and the parameters of the elastic cross section in the high energy part defined in Eq. (12), we fitted the experimental p-p and p-n cross sections [11,12]. In Fig. 1, we show the p-p (a) and p-n (b) total (solid line), elastic (long dashed line), and inelastic (dot-dashed line) cross sections. The inelastic cross section is the sum of the Δ (short dashed line) and N^* (dotted line) production cross sections, calculated by Eqs. (10), (12), (13), (15), and (16). In the same figure, we show the corresponding experimental total (open circles), elastic (open triangles), and inelastic (open boxes) cross sections [12] with error bars. For the p-p case, the present parametrization of elastic and inelastic cross sections fits the data for the whole energy range up to 3 GeV except for some deviation around 1 GeV, which is due to the elastic cross section and does not affect the result. On the other hand, for the p-n case where only the total cross section is available in the data, we fitted it at energies higher than 0.7 GeV up to 3 GeV, and adopt the Cugnon type elastic cross section in the low momentum region instead of the free elastic cross section.

In Fig. 2 we show the pion cross section of $pn \rightarrow nn\,\pi^+ + pp\,\pi^-$ (solid line) obtained by our new parametrization of Table II. In the same figure, the gray bold line denotes the result of the original parametrization of VerWest

and Arndt [13], while the experimental data are taken from Ref. [12]. With this new parameter set, our pion production cross section below 1.5 GeV does not differ very much from the original results of VerWest and Arndt [13], which are essentially the same as the data. However, above 1.5 GeV, our result fitted the experimental data, while the result obtained by extrapolating the original parametrization of VerWest and Arndt to higher energy shows a big bump, which has no experimental support.

In the higher energy region, the role of N^* becomes important. One of the good quantities which shows the characteristics of the higher resonances is the elementary two-pion production cross section. In the present prescription it is described only by σ_{N*} combined with the decay modes of the resonances which will be mentioned below. For example, it is shown in our prescription that

$$
\begin{aligned}
\sigma(pn \rightarrow pp\,\pi^0\pi^-) &= \tfrac{1}{15}\sigma_{N*}, \\
\sigma(pn \rightarrow pn\,\pi^+\pi^-) &= \tfrac{5}{12}\sigma_{N*}, \\
\sigma(pp \rightarrow pp\,\pi^+\pi^-) &= \tfrac{1}{3}\sigma_{N*}.
\end{aligned}
\qquad (17)
$$

We thus plot the σ_{N*} in Fig. 3 as well as the experimental two-pion production cross sections [12] scaled by the above factors. This figure shows that our parametrization fitted the gross features of the experimental data for the energy range up to 3 GeV. Although this parametrization should be modified if the two-Δ production channel or the direct two-pion decay of N^* or higher resonances is included, the present prescription of the elementary inelastic channels could roughly reproduce the experimental single- and two-pion production cross sections for the energy range up to 3 GeV.

We do not take into account the direct s-state pion production mechanism but all pions are assumed to be produced through baryonic resonances. The masses of the resonances are randomly distributed according to the Breit-Wigner distribution with a momentum-dependent width [14], i.e.,

$$
f(M) = \frac{0.25\Gamma^2}{(M - M_r)^2 + 0.25\Gamma^2}, \qquad (18)
$$
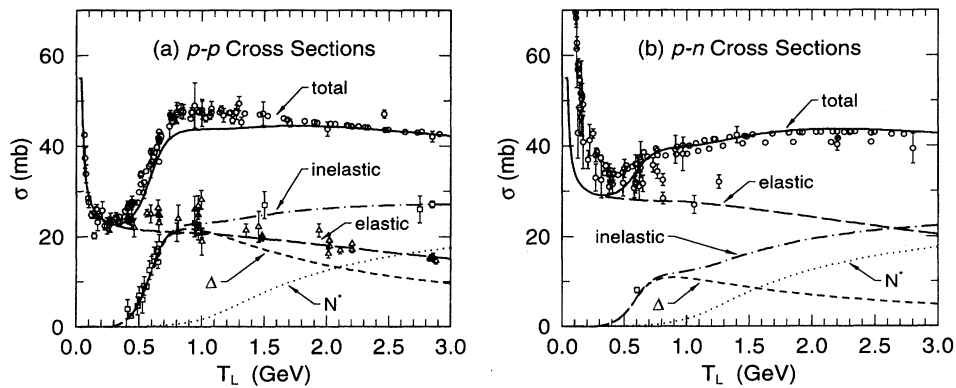
FIG. 1. p-p (a) and p-n (b) total (solid line), elastic (long dashed line), and inelastic (dot-dashed line) cross sections; the last is the sum of the Δ (short dashed line) and N^* (dotted line) production cross sections, calculated by Eqs. (10), (12), (13), (15), and (16). The experimental total (open circles), elastic (open triangles), and inelastic (open boxes) cross sections are taken from Ref. [12].
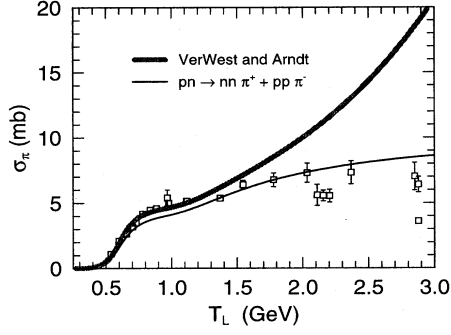
FIG. 2. Pion cross sections of $pn \rightarrow nn\pi^+ + pp\pi^-$ (solid line). The gray bold lines denote the results of the original parametrization of VerWest and Arndt [13], while the experimental data are taken from Ref. [12].

with

$$\Gamma = \left(\frac{q}{q_r}\right)^3 \frac{M_r}{M} \left(\frac{v(q)}{v(q_r)}\right)^2 \Gamma_r, \tag{19}$$

where q denotes the c.m. momentum in the πN channel, the index r refers to the values at the mass M_r, and

$$v(q) = \frac{\beta_r^2}{\beta_r^2 + q^2}. \tag{20}$$

We have applied this momentum-dependent width not only to the Δ resonance but also to $N^*(1440)$. The values of the parameters used in this paper are listed in Table III.

Another important ingredient of the resonance production [channels 2 and 4 in Eq. (9)] is the angular distribution of the resonances. Wolf *et al.* [9] parametrized the angular distribution of the experimental data [15] for $p + p \rightarrow n + \Delta^{++}$ and assumed the same angular dependence for each isospin channel in the following form:

$$g_R(s, \cos\theta) = a_0(s) [a_1(s) + 3a_3(s)\cos^2\theta], \tag{21}$$

with

$$a_0(s) = \frac{1}{4\pi[a_1(s) + a_3(s)]}. \tag{22}$$
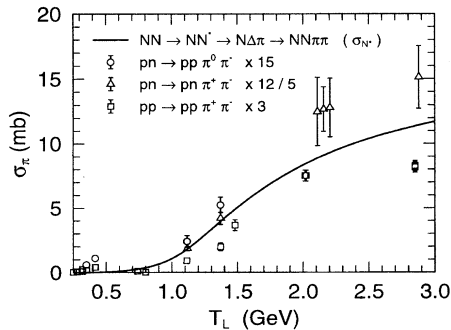
FIG. 3. Two pion production cross section. The solid line denotes σ_{N^*}, while the experimental data [12] are scaled according to the factors of Eq. (17).

TABLE III. Parameters in the width of resonances.

	M_r (MeV)	Γ_r (MeV)	β_r (MeV)
Δ	1232	110	300
N^*	1440	200	523

The values of $a_1(s)$ and $a_3(s)$ are given in Table IV. In the high energy region $\sqrt{s} > 2.4$ GeV, which corresponds to a laboratory energy higher than 1.2 GeV, this angular distribution is assumed to be constant, since there are no experimental data to be fitted in this energy region. However, above the resonance region $E_{lab} > 1.2$ GeV, this is not justified because, for example, the angular distribution of protons from the ^{27}Al(p, p') reaction at 3.17 GeV calculated by Eq. (21) deviates from the experimental data (cf. discussions on Fig. 9 in the next section).

In order to get a better parametrization for the high energy part, we assume that the angular dependence is effectively written as a sum of g_R and another term g_D as

$$g_A(s, \cos\theta) = \tfrac{1}{2} [g_R(s, \cos\theta) + g_D(s, \cos\theta)] \tag{23}$$

where

$$g_D(s, \cos\theta) = b_0(s) \exp[-2 p^2(s) b_1(s) (1 - \cos\theta)], \tag{24}$$

and

$$b_0(s) = \frac{p^2(s) b_1(s)}{\pi \{ 1 - \exp[-4 p^2(s) b_1(s)] \}}, \tag{25}$$

$$b_1(s) = \frac{0.14 s^2 [3.65 (\sqrt{s} - m_N - m_R)]^6}{1 + [3.65 (\sqrt{s} - m_N - m_R)]^6}, \tag{26}$$

$$p^2(s) = \frac{[s - (m_N - m_R)^2][s - (m_N + m_R)^2]}{4s}. \tag{27}$$

This form of g_D is obtained by modifying the Cugnon parametrization [1,4] of the NN elastic angular distribution so as to trace the angular distribution of Eq. (21) in the resonance region, and approach the elasticlike angular distribution for the higher momentum region. We use this angular distribution for Δ resonance and $N^*(1440)$. For the latter case, we apply this formula by shifting the energy $\sqrt{s}$ by the mass difference of the two resonances, i.e., 208 MeV. The energy dependence of this angular distribution is shown in Fig. 4, where we plot g_R (gray bold dashed lines) and g_D (solid lines) in (a), and g_R (gray bold dashed lines) and g_A (solid lines) in (b). In these figures, we symmetrized the elasticlike angular distribution, i.e., $(1/2)[g_D(s, \cos\theta) + g_D(s, -\cos\theta)]$, in order to compare it with the angular distribution of Eq. (21) (gray bold dashed lines). In the next

TABLE IV. Parameters in $f_R(s, \cos\theta)$.

$\sqrt{s}$ (GeV)	$\sqrt{s} \leq 2.14$	$2.14 < \sqrt{s} \leq 2.4$	$2.4 \leq \sqrt{s}$
$a_1(s)$	0.5	$29.03 - 23.75s + 4.865s^2$	0.06
$a_3(s)$	0.0	$-30.33 + 25.53s - 5.301s^2$	0.4
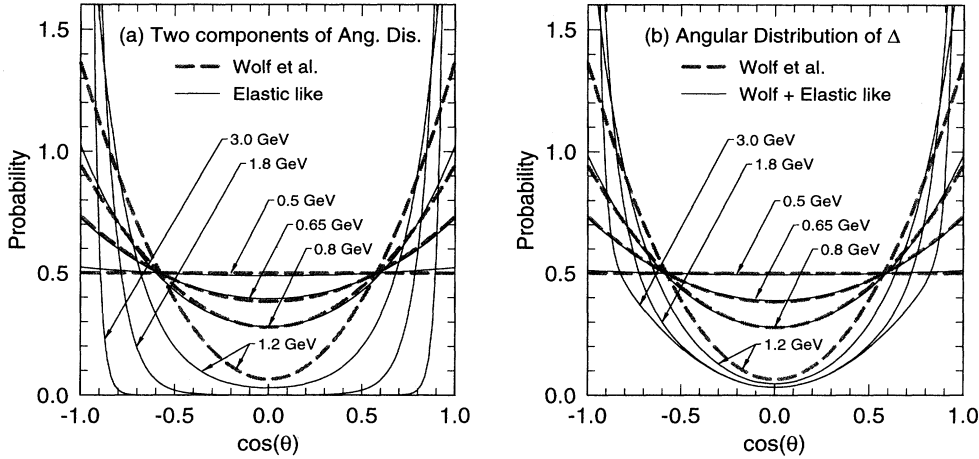
FIG. 4. The energy-dependent angular distribution of resonance production. (a) Two components of the angular distribution. The solid lines represent the elasticlike angular distributions of Eq. (24), $\frac{1}{2}$ $[g_D(s,\cos\theta)+g_D(s,-\cos\theta)]$, while the gray bold dashed lines are the resonancelike angular distributions of Eq. (21). (b) The total angular distribution of Δ (solid lines), which is the sum of g_R and g_D. The gray bold dashed lines are the same as in (a).

section, we will discuss the dependence of the final results of the (N, xN') reactions on this angular distribution of the hadronic resonances.

The cross sections for the channels 3 and 5 in Eq. (9) are determined by the law of detailed balance from the cross sections of channels 2 and 4, taking into account the mass dependence of the cross section [10].

For the pion absorption cross section on nucleons [channels 6 and 7 in Eq. (9)] we take the maximum cross sections from the particle data table [11] and scale them according to the Breit-Wigner formula. For the case of pion absorption on Δ [channel 8 in Eq. (9)], we assume the same cross section as in channel 7, shifting the energy by the mass difference of the Δ and nucleon.

Apart from the collision term, we take into account the decay of the baryonic resonances during the propagation as

$$9. \quad \Delta \rightarrow N + \pi,$$
$$10. \quad N^* \rightarrow N + \pi, \quad\quad\quad (28)$$
$$11. \quad N^* \rightarrow \Delta + \pi.$$
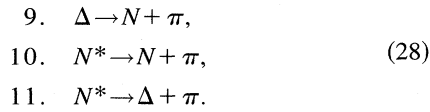
The decay probability of the resonances is determined by an exponential decay law using their momentum-dependent width Eq. (19) and their proper time. The decay is assumed to be isotropic in their rest frame. The branching ratio of the channels 10 and 11 of Eq. (28) is taken from the particle data table [11] as $\Gamma_{N^*\rightarrow\Delta+\pi}/[\Gamma_{N^*\rightarrow\Delta+\pi}+\Gamma_{N^*\rightarrow N+\pi}]=0.4$. The other branching ratios concerning their isospin are determined from the appropriate Clebsch-Gordan coefficients.

3. Relativistic corrections

The noncovariant framework is another problem in applying the QMD method to the reactions at higher bombarding energies. As explained above, we have already introduced the relativistic form of energy expression in the Hamiltonian Eq. (5) and adopted the relativistic kinematics in the collision term. However, a covariant formulation of the interaction term is necessary for a full relativistic description. A Lorentz-covariant extension of the QMD, dubbed relativistic quantum molecular dynamics (RQMD), has been proposed by Sorge *et al.* [16] based on the Poincaré-invariant constrained Hamiltonian dynamics. Although the RQMD is a numerically feasible extension of QMD toward a fully cova-

riant approach, it still costs too much computing time to apply the RQMD model to heavy systems. We thus make the following alternative extension of QMD and include the main part of the relativistic dynamical effects in our model.

Lehmann *et al.* [17] have compared the time evolution of the phase space and the particle production obtained by QMD and RQMD, looking for relativistic effects in heavy-ion collisions in the intermediate energy regime. They found that there is no significant difference between the results of QMD and RQMD in the η and π meson production cross sections [17] and the proton inclusive spectra [18]. The difference appeared only in the values of the maximum density [18] and the transverse flow [19]. Both are larger in RQMD. Their studies showed that a large part of the difference comes from the Lorentz contraction of the initial phase space distribution in RQMD. If this Lorentz contraction is employed in the normal QMD, however, the transverse flow is overestimated. Thus they concluded that in RQMD this effect is partially counterbalanced by the covariant treatment of the interaction, but there still remains an increased flow compared with the normal QMD calculation. Based on their investigation, we introduce in this paper Lorentz-scalar quantities into the arguments of the interactions in Eq. (5) as well as a Lorentz contraction of the initial phase space distribution. By these modifications the main part of the relativistic dynamical effects would be approximately included in our QMD.

All arguments of the interaction in Eq. (5) are written as a function of the squared spatial distance:

$$\mathbf{R}_{ij}^2 = (\mathbf{R}_i - \mathbf{R}_j)^2. \quad\quad\quad (29)$$

In the RQMD [17,18], these arguments are replaced by the squared transverse four-dimensional distance $-q_{T_{ij}}^2$ defined as

$$-q_{T_{ij}}^2 = -q_{ij}^2 + \frac{(q_{ij}\cdot p_{ij})^2}{p_{ij}^2}, \quad\quad\quad (30)$$

where q_{ij} is the four-dimensional distance $q_i - q_j$, while p_{ij} denotes the sum of the four momenta of the two particles $p_i + p_j$. In the c.m. system of the particles i and j, the squared covariant transverse distance $-q_{T_{ij}}^2$ reduces to the

usual squared distance. We therefore change the argument in Eq. (5) from $\mathbf{R}_{ij}^2$ to the squared distance in the c.m. system of the two particles $\tilde{\mathbf{R}}_{ij}^2$, where the tilde means the quantities defined in the c.m. system of the two particles,

$$\tilde{\mathbf{R}}_{ij}^2 = \mathbf{R}_{ij}^2 + \gamma_{ij}^2 (\mathbf{R}_{ij} \cdot \boldsymbol{\beta}_{ij})^2 , \tag{31}$$

with

$$\boldsymbol{\beta}_{ij} = \frac{\mathbf{P}_i + \mathbf{P}_j}{E_i + E_j}, \qquad \gamma_{ij} = \frac{1}{\sqrt{1 - \boldsymbol{\beta}_{ij}^2}} . \tag{32}$$

By this change, all interactions of the Hamiltonian [Eq. (5)] depend also on the momentum. The form of the equation of motion [Eq. (4)] changes to

$$\dot{\mathbf{R}}_i = \frac{\mathbf{P}_i}{\sqrt{m_i^2 + \mathbf{P}_i^2}} + \sum_j D_{ij} \frac{\partial \tilde{\mathbf{R}}_{ij}^2}{\partial \mathbf{P}_i} , \tag{33}$$

$$\dot{\mathbf{P}}_i = -\sum_j D_{ij} \frac{\partial \tilde{\mathbf{R}}_{ij}^2}{\partial \mathbf{R}_i} , \tag{34}$$

with

$$D_{ij} = -\frac{1}{2} \frac{A}{\rho_0} \frac{1}{2L} \rho_{ij} - \frac{1}{1+\tau} \frac{B}{\rho_0^\tau} \frac{\tau}{2} (\langle \rho_i \rangle^{\tau-1} + \langle \rho_j \rangle^{\tau-1}) \frac{1}{2L} \rho_{ij}$$

$$+ \frac{e^2}{2} c_i c_j \left\{ -\frac{1}{|\tilde{\mathbf{R}}_{ij}|} \mathrm{erf}\left(\frac{|\tilde{\mathbf{R}}_{ij}|}{\sqrt{4L}} \right) + 8\pi L \rho_{ij} \right\} \frac{1}{\tilde{\mathbf{R}}_{ij}^2}$$

$$- \frac{C_s}{2\rho_0} (1 - 2|c_i - c_j|) \frac{1}{2L} \rho_{ij} \tag{35}$$

and

$$\frac{\partial \tilde{\mathbf{R}}_{ij}^2}{\partial \mathbf{R}_i} = 2\mathbf{R}_{ij} + 2\gamma_{ij}^2 (\mathbf{R}_{ij} \cdot \boldsymbol{\beta}_{ij}) \boldsymbol{\beta}_{ij} , \tag{36}$$

$$\frac{\partial \tilde{\mathbf{R}}_{ij}^2}{\partial \mathbf{P}_i} = \frac{2\gamma_{ij}^2}{E_i + E_j} (\mathbf{R}_{ij} \cdot \boldsymbol{\beta}_{ij}) \left\{ \mathbf{R}_{ij} + \gamma_{ij}^2 (\mathbf{R}_{ij} \cdot \boldsymbol{\beta}_{ij}) \left(\boldsymbol{\beta}_{ij} - \frac{\mathbf{P}_i}{E_i} \right) \right\} , \tag{37}$$

where ρ_{ij} is defined in Eq. (7).

We also introduce the Lorentz-scalar quantities into the one-body phase space distribution function Eq. (3) as

$$f_{ij} = 8 \exp\left[-\frac{1}{2L} \tilde{\mathbf{R}}_{ij}^2 - \frac{2L}{\hbar^2} \tilde{\mathbf{P}}_{ij}^2 \right] , \tag{38}$$

where $\tilde{\mathbf{P}}_{ij}^2$ denotes the squared relative momentum in the c.m. system of the particles i and j, which is expressed for two particles with the same mass as

$$\tilde{\mathbf{P}}_{ij}^2 = \mathbf{P}_{ij}^2 - (E_i - E_j)^2 , \tag{39}$$

with

$$\mathbf{P}_{ij} = \mathbf{P}_i - \mathbf{P}_j . \tag{40}$$

At the starting point of the QMD calculation, we boost the ground state of the projectile (and the target as well if the

c.m. system of the target and projectile is chosen as the reference frame) according to the beam energy. The coordinate $\mathbf{R}_{iz}^b$ and momentum $\mathbf{P}_{iz}^b$ of the nucleon in the beam direction z after the boost are obtained by Lorentz transformation from those before the boost, $\mathbf{R}_{iz}$ and $\mathbf{P}_{iz}$, as

$$\mathbf{R}_{iz}^b = (\mathbf{R}_{iz} - \mathbf{R}_{0z}) / \gamma + \mathbf{R}_{0z} , \tag{41}$$

$$\mathbf{P}_{iz}^b = \gamma (\mathbf{P}_{iz} + \beta E_i) , \tag{42}$$

where $\mathbf{R}_0$ denotes the initial c.m. coordinate of the nucleus, while β and γ are the boosting velocity and its gamma factor, respectively. At this moment, the potential energy of the system and the phase space distribution function keep the same values as those before the boost due to their Lorentz-scalar properties discussed above. During the propagation of the boosted nuclei, however, those quantities are changing slightly even in the above prescriptions, since the equations of motion Eq. (33) and (34) are not covariant. But the disturbance due to the noncovariant feature of the equation of motion is negligibly small up to the energy 3 GeV/nucleon. We thus introduce the relativistic corrections discussed above to the noncovariant QMD to save computing time instead of using the full covariant framework.

We should mention here that if one employs the Lorentz contraction for the boosted initial state but does not replace the arguments of the interaction and phase space distribution by the Lorentz-scalar ones, the potential energy decreases about 80 MeV and the phase space factor at each nucleon's point changes by about 40% after the boost in the case of ^{40}Ca even at 1 GeV/nucleon boosting energy. This means that the boosted ground state obtained in this way may decay spontaneously before it collides with the other nucleus. By our prescription, we are free from this problem.

We have checked the above prescription by analyzing the transverse flow, which is sensitive to the treatment of the relativity as discussed in Ref. [17]. In Fig. 5 we show the energy dependence of so called directed transverse momentum $\langle \mathbf{P}_x^{\mathrm{dir}} \rangle$, which is a measure for the transverse flow and defined by

$$\langle \mathbf{P}_x^{\mathrm{dir}} \rangle = \frac{1}{N} \sum_{i=1}^N \mathrm{sgn}[Y_{\mathrm{c.m.}}(i)] \mathbf{P}_{ix} , \tag{43}$$

where $Y_{\mathrm{c.m.}}(i)$ is the rapidity of the ith baryon in the c.m. system and $\mathbf{P}_{ix}$ its transverse momentum in the reaction plane. We plot the result of the present QMD simulation (solid line with full boxes) as the difference from that of RQMD [18] for ^{40}Ca + ^{40}Ca reactions at $b = 2$ fm, for the energy range from 150 MeV/nucleon to 4 GeV/nucleon. In these calculations, we use the same ground states (mentioned below), the same Gaussian wave packets, and the same interaction (mentioned before). We omitted the Coulomb interaction and two-body collision term for simplicity. In Fig. 5, we also plot the other results obtained by standard QMD (dot-dashed line with open circles) without the initial Lorentz contraction and without the relativistic corrections, and by standard QMD only with the Lorentz contraction (dashed line with open boxes). As mentioned before, the Lorentz contraction of the initial phase space distribution increases the flow, which is shown by the change from the dot-dashed line
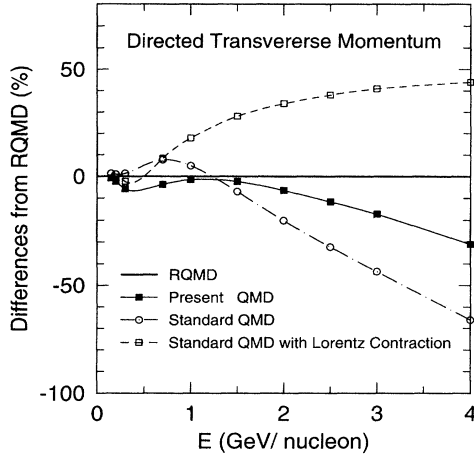
FIG. 5. The directed transverse momentum as a function of energy/nucleon for the ^{40}Ca+^{40}Ca reaction at $b = 2$ fm. The results are shown as the differences from that of the RQMD [18]. The solid line with full boxes denotes the result of the present model with the relativistic corrections and the initial Lorentz contraction. The dot-dashed line with open circles is the result of the standard QMD without the initial Lorentz contraction and without the relativistic corrections, while the dashed line with open boxes is the result of the standard QMD only with the initial Lorentz contraction.

to the dashed line. By the full covariant treatment of the interaction, however, this effect is counterbalanced, but an increased flow still remains [17]. As seen in Fig. 5, our pre-scription does not deviate very much from the full covariant treatment up to 3 GeV/nucleon. We thus expect that our QMD simulation with the relativistic corrections is very close to the covariant simulation RQMD in this energy re-gime.

At much higher energy, however, our result decreases lin-early from that of RQMD. This deviation comes from the different treatment of the potential between the RQMD [18] and our QMD; a Lorentz-scalar type in the former, and a time component of the vector type in the latter. This is un-derstood qualitatively by considering a single-particle mo-tion under a fixed external potential U. In the Lorentz-scalar treatment of the potential U, the single-particle energy p_i^0 is expressed in this simple case as

$$p_i^0 = \sqrt{p_i^2 + m_i^2 + 2m_i U}. \tag{44}$$

Accordingly the equation of motion is

$$\dot{\mathbf{P}}_i = -\frac{m_i}{p_i^0} \frac{\partial U}{\partial \mathbf{R}_i}. \tag{45}$$

On the other hand, in our prescription they are

$$p_i^0 = \sqrt{p_i^2 + m_i^2} + U \tag{46}$$

and

$$\dot{\mathbf{P}}_i = -\frac{\partial U}{\partial \mathbf{R}_i}. \tag{47}$$

In this test calculation, the form of $\partial U/\partial \mathbf{R}_i$, which is attrac-tive in the beginning, is almost the same in our QMD and in the RQMD. Thus the force of our QMD becomes larger and deviates linearly from that of the RQMD as the energy in-creases. Above 3 GeV/nucleon, therefore, the full covariant prescription is necessary to describe the reactions, particu-larly the nucleus-nucleus collisions. This is out of the scope of this paper.

Some details of actual numerical calculations should be mentioned here, since all potential terms depend on the mo-mentum by the relativistic corrections. In order to keep nu-merical accuracy, we use the second-order Runge-Kutta method to integrate the equations of motion. For the energy conservation for the collision term, we assume

$$E_i + E_j + U_{\text{pot}} = E_i' + E_j' + U_{\text{pot}}', \tag{48}$$

where E_i, E_j, and E_i', E_j' are the energies of particles i and j before and after the collision, while U_{pot} and U_{pot}' are the potential energy of the system. We determine iteratively the final momenta of the colliding particles so as to satisfy the energy conservation Eq. (48). This prescription is applied to the channels 1–5 in Eq. (9) and 9–11 in Eq. (28). For the pion absorption channels 6, 7, and 8 in Eq. (9), the energy conservation is written as

$$E_i + E_j + U_{\text{pot}} = E_R + U_{\text{pot}}', \tag{49}$$

where E_R is the resonance energy. In this case, we determine iteratively the rest mass of the resonance to conserve the energy.

4. Properties of "ground state"

An important ingredient of the QMD calculation is how to determine the initial phase space distribution of the projectile and target. For that we cannot use the real ground state (en-ergy minimum state) of the system defined by the Hamil-tonian Eq. (5), since the model does not have fermionic properties. However, it is necessary to obtain a stable "ground state." Also some typical properties of the real ground state should approximately be fulfilled, especially the binding energy and phase space distribution. To get such a "ground state," we employ the following random packing procedure [8].

We distribute the centers of position $\mathbf{R}_i$ of the individual Gaussian wave packet according to a distribution of the Woods-Saxon shape with the radius $R_0 = 1.124A^{1/3} - 0.5$ fm and the diffuseness parameter $a = 0.2$ fm. We cut off the Woods-Saxon tail at $R_{\text{max}} = 1.124A^{1/3}$ fm. In this procedure, we impose a minimum distance between the centers of the Gaussians in order to reduce the density fluctuation. We use 1.5 fm for identical nucleons and 1.0 fm for the others.

Now we can calculate the density and potential energy at any point (here, we do not need the relativistic correction discussed in the previous subsection). Then the center of momentum $\mathbf{P}_i$ is randomly sampled from the sphere of radius $p_F(\mathbf{R}_i)$ which is the Fermi momentum obtained by the local Thomas-Fermi approximation. This sampling is rejected and another value is sampled if the sum of kinetic and potential energy of the particle is positive or the phase space factor $f(\mathbf{R}_j, \mathbf{P}_j)$ [cf. Eqs. (2) and (3)] for the nucleon j which have
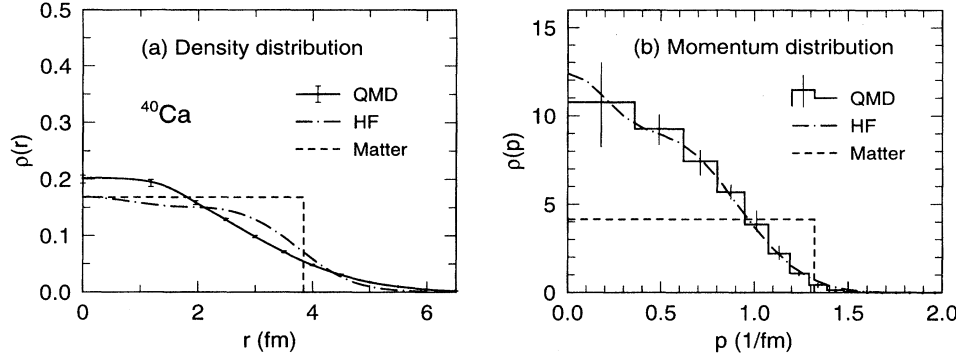
FIG. 6. (a) Density distribution $\rho(r)$ and (b) momentum distribution $\rho(p)$ of the ground state of ^{40}Ca obtained by QMD simulation (solid lines) averaged over time evolution up to 200 fm/c and over 100 events. The error bars denote the fluctuations in time evolution averaged over 100 events. The dot-dashed lines show the results of Hartree-Fock calculations, while the dashed lines denote the limit of infinite nuclear matter.

been previously accepted violates the Pauli principle [8].

Finally, we check the total binding energy with the simple mass formula [20], i.e.,

$$E_{\rm bin} = -15.56A + 17.23A^{2/3} + 46.57\frac{(N-Z)^2}{2A}$$
$$+\frac{3}{5}\frac{Z^2 e^2}{1.24A^{1/3}}.\tag{50}$$

If the binding energy per nucleon obtained by our sampling lies within $E_{\rm bin}\pm 0.5$, we adopt this configuration as a "ground state."

Thus the "ground state" obtained by this procedure always has an appropriate binding energy. However, there is still open phase space below the Fermi surface, since the "ground state" is not the energy minimum state of the fermions. In fact, during the time evolution of the "ground state" under the QMD dynamics described in the previous subsection, only 70% of the collisions are blocked by the final state Pauli blocking in the two-body collision term. It is allowed at a collision that one nucleon goes down to the lower energy state and the other goes up to the positive energy state. This means that some nucleons could be spontaneously emitted after some time due to the fluctuation of the configuration. To avoid this problem, we assume from a technical point of view that any pair of nucleons originating in the same nucleus do not collide with each other until at least one of them experiences a collision with a nucleon from the other nucleus. By this assumption the number of emitted nucleons from the "ground state" is reduced to less than about 1% of the nucleons up to the time 200 fm/c.

The density profile of the "ground state" obtained here has high density in the center and a rather wide surface shape. This is due to the large width of the Gaussian $L=2.0$ fm^2 used in this paper. On the other hand, the momentum distribution of the "ground state" well reproduces the result of a Hartree-Fock calculation. In Fig. 6, we show (a) the density distribution $\rho(r)$ and (b) the momentum distribution $\rho(p)$ for the "ground state" of ^{40}Ca obtained by QMD simulation (solid lines). The results shown here are averaged quantities over time evolution up to 200 fm/c and over 100 events. The error bars in Fig. 6 denote the fluctuations in time evolution averaged over 100 events. Although the fluctuation of one event is much larger, this figure shows that the ground state profile is very stable in time on the

average over the events. In the same figure, we also plot the results of a Hartree-Fock calculation (dot-dashed lines) and the limit of infinite nuclear matter (dashed lines). The energy spectra of the emitted particles given in the next section, particularly of the subthreshold particle production [21], are more sensitive to the momentum distribution than the density profile. This is the reason why we adopted a parametrization which leads to a better momentum distribution at the cost of a diffuse density profile.

B. Statistical decay model

At the end of the dynamical stage of the reaction, the QMD simulation yields many fragments, which are normally in highly excited states. One may think that the decay process of the excited fragments might be described by QMD dynamics if we can continue the calculation for a long enough time. However, we do not follow this method but instead we stop the QMD calculation and switch to the statistical decay model (SDM) at the end of the dynamical stage. There are two reasons for this hybrid model. One is that the time scales of the dynamical and statistical processes are quite different. It is not clever or even practically impossible to continue a reliable QMD calculation for more than 10^{-20} sec, which is necessary to calculate the decay process. Another is a more fundamental reason that the Fermi statistics, which is essential to describe the decay process of the fragments, cannot be traced correctly in the QMD simulation [22].

We identify the fragments together with their excitation energies at about 100–150 fm/c of the QMD simulation. The dependence of the final results on this switching time will be discussed in the next section. Each fragment is recognized by using a minimum distance chain procedure, i.e., two nucleons are considered to be bound in a fragment if the distance between their centroids is smaller than 4 fm. We then calculate the total energy of the fragment in its rest frame and estimate the excitation energy by subtracting the ground state energy given by Eq. (50).

Though many sophisticated statistical decay codes have been proposed so far, we use here the simple model of light-particle evaporation. We consider only n, p, d, t, ^{3}He, and α evaporation. The emission probability P_x of these particles x is given with the Fermi gas model as

$$P_x = (2J_x + 1)\ m_x\ \epsilon\ \sigma_x(\epsilon)\ \rho(E)\ d\epsilon,\tag{51}$$

where J_x, m_x, and ϵ are the spin, mass, and kinetic energy of the particle x, while $\sigma_x(\epsilon)$ and $\rho(E)$ denote the inverse cross section for the absorption of the particle with energy ϵ and the level density of the residual nucleus with the excitation energy E, respectively. We use the following simple form for $\rho(E)$:

$$\rho(E) = w_0 \exp(2\sqrt{aE}), \tag{52}$$

with $a = A/8$ MeV^{-1} and w_0 a constant. The inverse cross section is assumed to have the form

$$\sigma_x(\epsilon) = \begin{cases} (1 - U_x/\epsilon) \, \pi R^2, & \epsilon > U_x \\ 0, & \epsilon \leq U_x, \end{cases} \tag{53}$$

where R denotes the absorption radius and U_x is the Coulomb barrier for the particle x, for which we employ empirical values used in the existing statistical decay code [23]. The excitation energy E in Eq. (52) is given by

$$E = E_0 - \epsilon - Q, \tag{54}$$

where E_0 denotes the excitation energy of the parent nucleus and Q is the reaction Q value calculated from the mass formula Eq. (50). The total emission probability R_x of the particle x is obtained by integrating the available energy of Eq. (51) as

$$R_x = (2J_x + 1) \, m_x \int_{U_x}^{E_0 - Q_x} \epsilon \, \sigma_x(\epsilon) \, \rho(E_0 - Q_x - \epsilon) \, d\epsilon. \tag{55}$$

This integration can be calculated analytically and the energy spectrum of the emitted particles is given by

$$N(\epsilon_x) \, d\epsilon_x = \frac{\epsilon_x - U_x}{T_x^2} \exp\left\{ -\frac{\epsilon_x - U_x}{T_x} \right\} \, d\epsilon_x, \tag{56}$$

with

$$a \, T_x^2 = E_0 - U_x - Q_x. \tag{57}$$

In this formulation, we do not consider the γ decay nor the angular momentum dependence. The latter is important for heavy-ion reactions but not so serious for the nucleon-induced reactions considered in this paper. We simulate the whole statistical decay process as a sequential light-particle evaporation discussed above by making use of the Monte Carlo method until no more particles can be emitted.

III. ANALYSIS OF THE (N, xN') REACTIONS

In this section, we systematically apply the QMD plus SDM method described in the previous section to (N, xN') (nucleon in, nucleon out) type reactions. In order to get sufficient statistics, we performed the QMD calculations for a large number of events, typically 50 000 events, and averaged them to obtain the following results.

We first check the dependence on the switching time t_{sw} when the QMD calculation is stopped and switched to SDM, which is an ambiguous point of the present model. In Fig. 7, we show a typical neutron energy spectrum at 30° laboratory
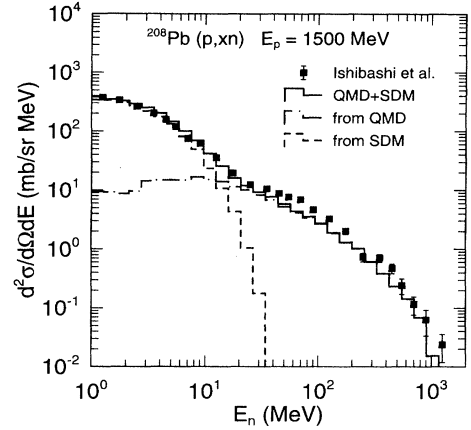
FIG. 7. Neutron energy spectrum at the 30° laboratory angle for the reaction $p(1.5 \text{ GeV}) + {}^{208}\text{Pb}$. The experimental data (full boxes with error bars) are taken from Ref. [24]. The solid line denotes the final result of the QMD + SDM calculation with the switching time $t_{sw} = 100$ fm/c. The dot-dashed line is the result obtained only by the QMD calculation up to 100 fm/c, while the dashed line is the neutron spectrum coming from the QMD fragments calculated with the SDM.

angle for the reaction $p(1.5 \text{ GeV}) + {}^{208}\text{Pb}$. Note that the x axis is plotted in the logarithmic scale to compare the calculated results in detail with the experimental data particularly in the low energy region. The experimental data (full boxes with error bars) are taken from Ref. [24]. The solid histogram denotes the final result of the QMD + SDM calculation. In this case, we switch the QMD calculation to SDM at 100 fm/c. In the same figure, we also plot the spectrum of the neutron obtained only by QMD calculation up to 100 fm/c (dot-dashed histogram) and that coming from the QMD fragments calculated with SDM (dashed histogram), respectively. The former shows a cascade and/or preequilibrium energy spectrum, and the latter an evaporation spectrum. These two components of the spectrum are affected by changing the switching time t_{sw}. However, the total spectrum shape, which is the sum of the two components, stays almost unchanged if an adequately long time is chosen for the switching time t_{sw}. This is shown in Fig. 8, where we plot results of the total spectra calculated by QMD + SDM with three different switching times, 50 fm/c (dashed line), 100 fm/c (solid line), and 150 fm/c (dot-dashed line). This figure shows that, although the latter two lines resemble each other, they deviate definitely from the first line. This indicates that the QMD fragments before 100 fm/c are not in thermal equilibrium and that within a time interval from 100 fm/c to 150 fm/c the decay processes of the excited fragments described by QMD and SDM are nearly equivalent. Although we should keep in mind that these two are not identical at low temperature as the former is always dominated by the classical statistics [22], we can conclude that the final results are not sensitive to the switching time t_{sw} as long as it is chosen after the time when thermal equilibrium is achieved and before the time the temperature of the fragments becomes low and classical statistics breaks down seriously. A similar conclusion has been obtained in Ref. [6],
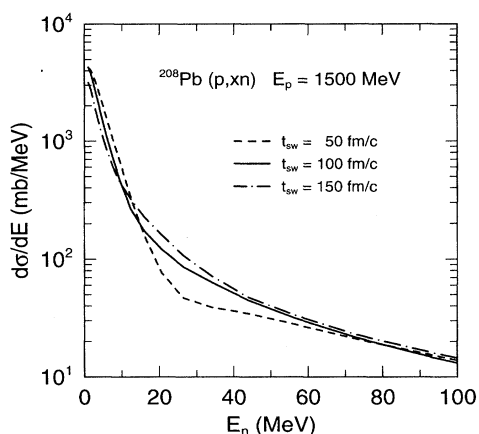
FIG. 8. The total energy spectra calculated by QMD + SDM with different switching times $t_{sw} = 50$ fm/c (dashed line), $t_{sw} = 100$ fm/c (solid line), and $t_{sw} = 150$ fm/c (dot-dashed line). The reaction system is the same as in Fig. 7.

which indicates that the minimum switching time to get stable results depends on the size of the system and the incident energy. For the case of nucleon-induced reactions, we found that 100 fm/c is enough to get stable results and we use this value for all systems in the present study.

The next check is the detailed examination of the inelastic channels in the two-body collision term. For this purpose we compare our results with the experimental data at high incident energy of protons on the light-mass target, which directly reflects the elementary processes included in the model. In Fig. 9, we plot the invariant cross section of the proton (left-hand side) and negative pion (right-hand side) emission for the reaction p (3.17 GeV) $+ {}^{27}$Al. The experi-

mental data (full boxes with error bars) are taken from Ref. [25] and the results of QMD + SDM are denoted by solid histograms. In the same figure, we plot the results of QMD + SDM with different choices of the angular distribution of the resonances. The dashed histograms are the results obtained with only the resonancelike angular distribution of Eq. (21), while the dot-dashed histograms are those with the directlike angular distribution of Eq. (24). This figure shows that the average of the two components of the angular distribution of Eq. (23) well fits the experimental proton spectra. On the other hand, the pion spectra are rather insensitive to the angular distribution of the resonances. Instead, their spectra are predominantly determined by the mass distribution of the resonances of Eq. (18). Although the authors of Ref. [25] analyzed these data by making use of the two-moving-source model, our QMD + SDM can reproduce excellently the proton and pion spectra at the same time without any special assumption.

In Figs. 10–15, we compare the neutron energy spectra obtained by the QMD + SDM calculations with the experimental data [24,26] for Fe and Pb targets at proton energy from 113 MeV up to 3 GeV. In the fields of application of accelerators, such as spallation neutron sources, accelerator-based transmutation systems, and shielding of cosmic rays in space activity, the production of slow neutrons plays an important role. That is the reason we chose these data [24,26] to compare with, since the neutron spectra from 1 MeV up to the beam energy are available. For efficient comparisons of the calculations and the data, both for low energy and high energy regions, we plot the same results in two figures with the x axis in a logarithmic scale (left-hand side) and in a linear scale (right-hand side). One can see the detail of the thermal and preequilibrium neutron spectra in the former figure, and the directlike components of the spectra in the latter figure.
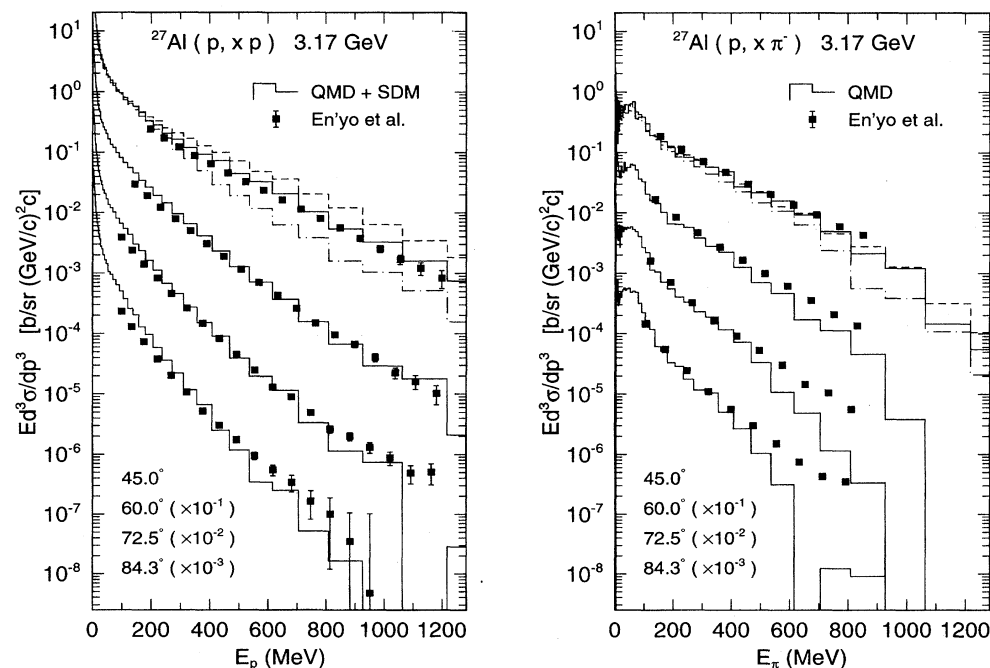
FIG. 9. Invariant cross sections of the proton (left-hand side) and negative pion (right-hand side) emission for the reaction p(3.17 GeV) $+ {}^{27}$Al at different laboratory angles as indicated in the figure. Full boxes with error bars are the experimental data taken from Ref. [25] and the results of QMD + SDM are denoted by solid histograms. The dashed histograms are results of another QMD + SDM obtained with only the resonancelike angular distribution Eq. (21), while the dot-dashed histograms are obtained with the directlike angular distribution Eq. (24).
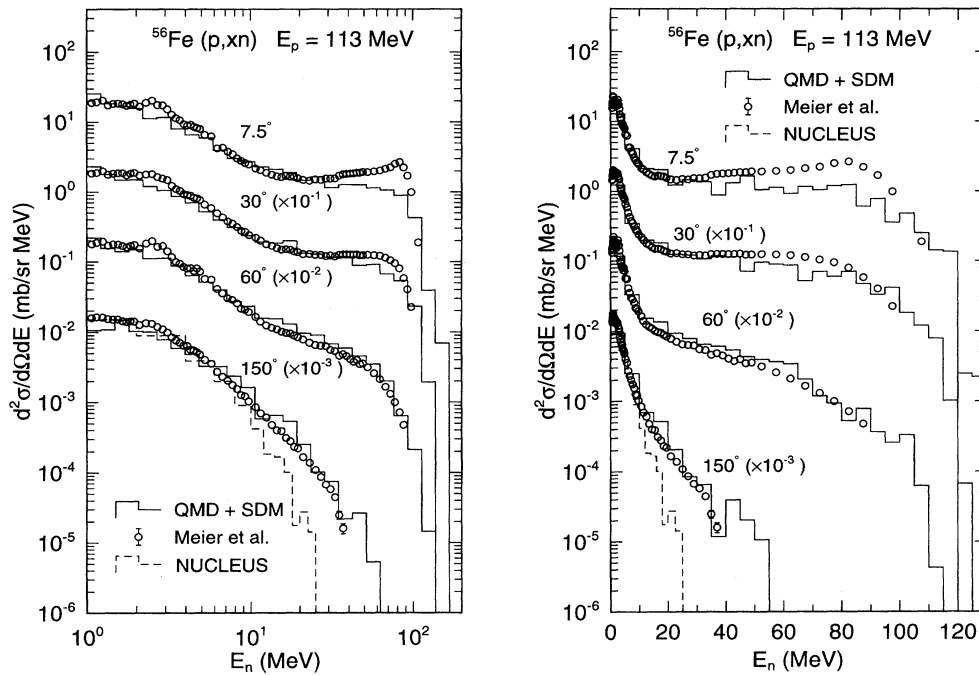
FIG. 10. Neutron energy spectra for the reaction p (113 MeV) $+ ^{56}$Fe at different laboratory angles as indicated in the figure. The x axis is plotted in a logarithmic scale on the left-hand side, and a linear scale on the right-hand side. The solid histograms are the results of QMD + SDM and the open circles with error bars denote the experimental data taken from Ref. [26]. The dashed histograms denote the results of NUCLEUS [27] at the 150° laboratory angle.

These figures indicate that over a broad range of incident energies from 100 MeV to 3 GeV, independently for the targets, and of all angles of the outgoing neutrons, our results for the neutron energy spectra agree well with the data from 1 MeV up to the beam energy. Though one may notice some disagreement at the high energy part of the most forward angle, which will be discussed later, the overall agreement is satisfactory. In particular, a remarkable agreement of the present calculations with the low energy neutron data below

several tens of MeV confirms that the QMD gives proper excitation spectra of the excited fragments from which the statistical neutron emission takes place. With a suitable chosen fixed set of parameters, our QMD plus SDM model is able to reproduce quantitatively the overall neutron spectra for the broad range of incident energies and target masses.

At 113 MeV, we additionally compare our results with the prediction of the intranuclear cascade plus light-particle evaporation model (NUCLEUS) [27]. This model is essentially
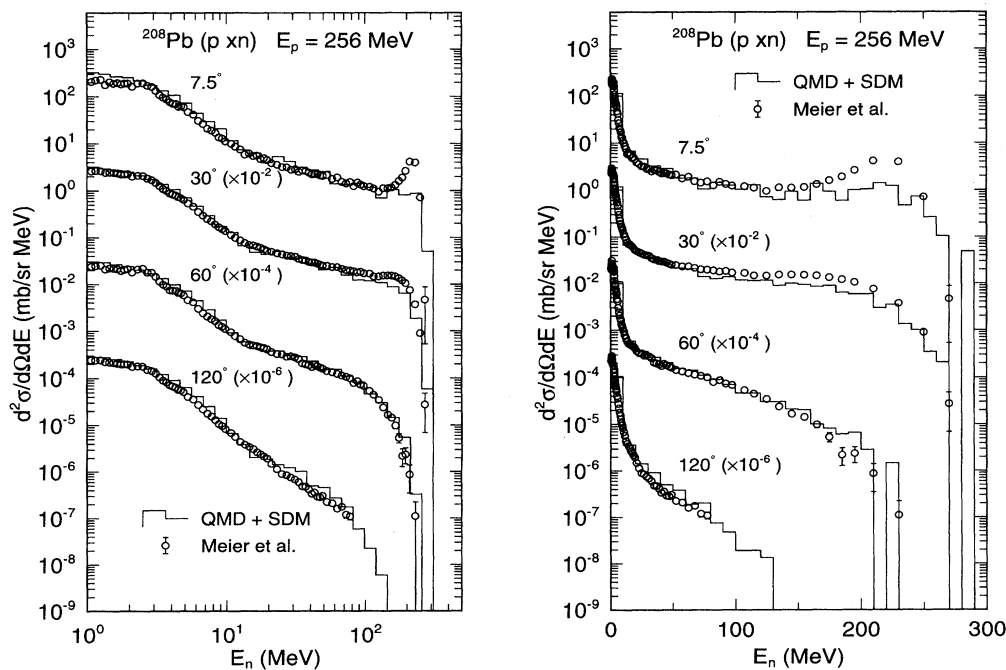
FIG. 11. Same as Fig. 10 for the reaction p (256 MeV)$+ ^{208}$Pb.
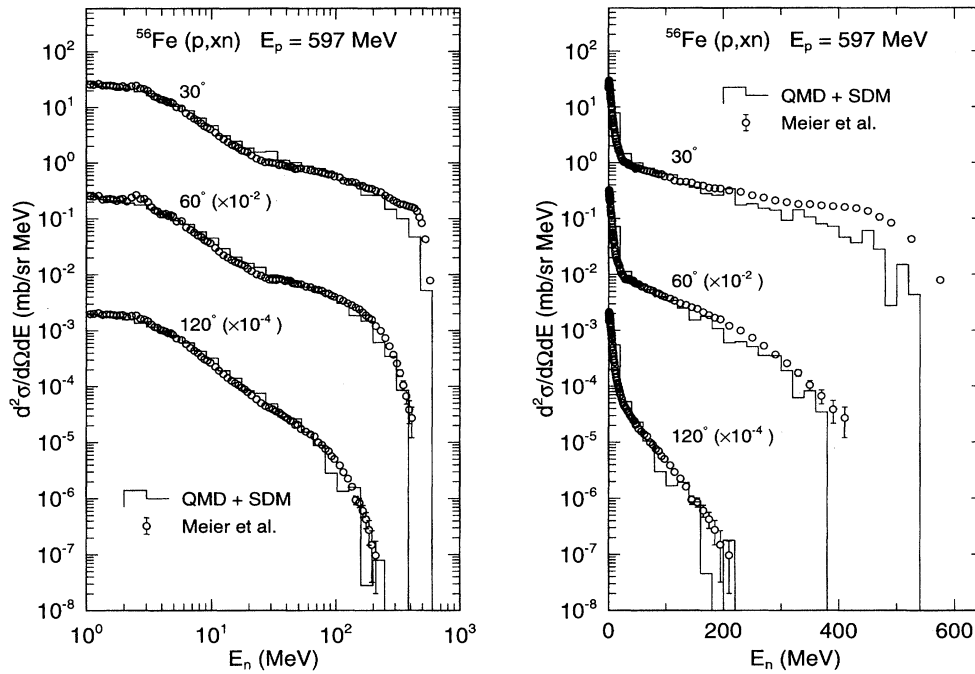
FIG. 12. Same as Fig. 10 for the reaction p (597 MeV)$+^{56}$Fe.

the intranuclear reaction part of the NMTC [28] and HETC [29] codes. Calculations with NUCLEUS yield almost the same results as ours in the forward angles but give lower values in the backward angle, which is denoted by the dashed histogram at 150° in Fig. 10. In this energy regime it has been reported [30,31] that the semiclassical preequilibrium models based on an intranuclear cascade model also fail to reproduce the angular distributions. We found from detailed compari-

son of the calculations that the underestimation of the backward angle in the above models is due to the insufficient treatment of the soft interaction of a nucleon with all the rest of the nucleons in the nucleus, which is naturally included in the QMD formalism.

One may think that this explanation is in contradiction with Refs. [5,32] where the authors attribute the failure to insufficient contributions from second- and higher-order col-
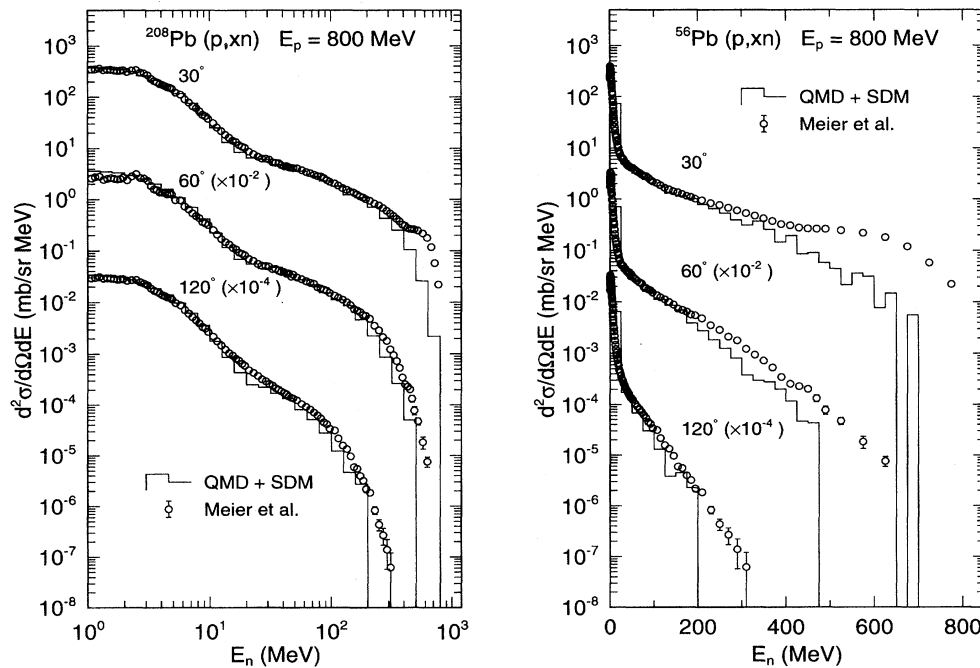
FIG. 13. Same as Fig. 10 for the reaction p (800 MeV)$+^{208}$Pb.
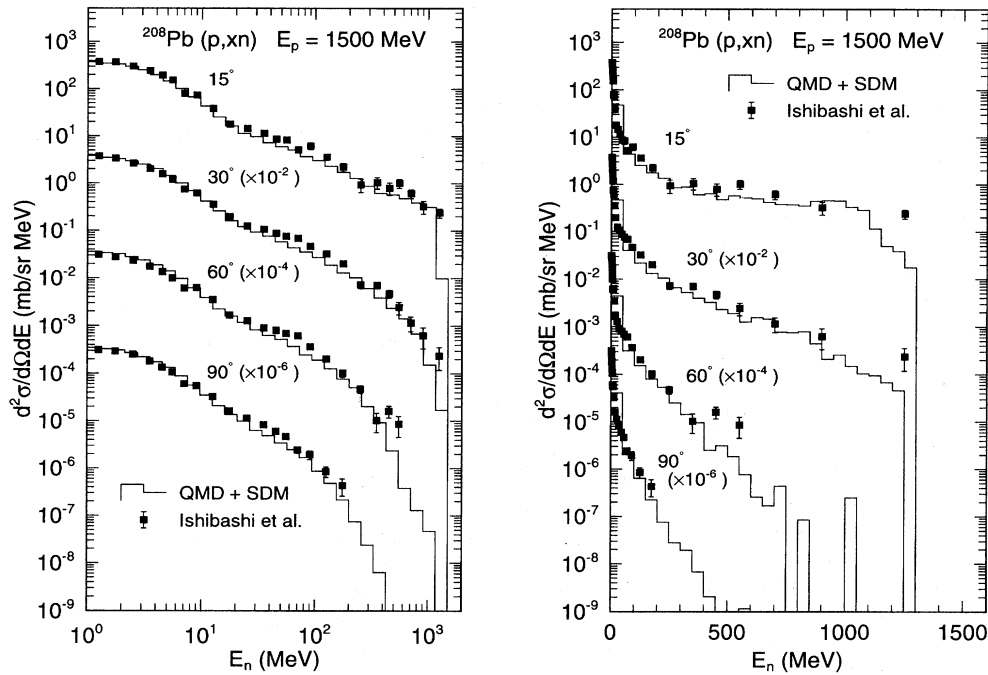
FIG. 14. Same as Fig. 10 for the reaction p (1500 MeV) $+ ^{208}$Pb. The full boxes with error bars are the experimental data taken from Ref. [24].

lisions. To resolve this problem, we have checked that NUCLEUS has almost the same prescription of hard nucleon-nucleon interaction and almost the same momentum distribution in the ground state as QMD. The difference is that our QMD part includes the soft nucleon-nucleon interaction but NUCLEUS does not. This soft interaction diffracts the nucleon. As a result, the yields of the backward angle increase and for the same reason the number of multiple hard collisions also increases.

On the other hand, the multistep model of Feshbach-Kerman-Koonin (FKK) [33] has been also applied to the energy regime around 100 MeV [32]. Although the FKK approach successively reproduced the angular distribution, the overall absolute values of their results are very sensitive to the strength parameter of the residual interaction, which is adjusted to fit the experimental data. The strength so determined depends on the incident particle, target nucleus, and incident energy. In QMD, on the contrary, the parameters of
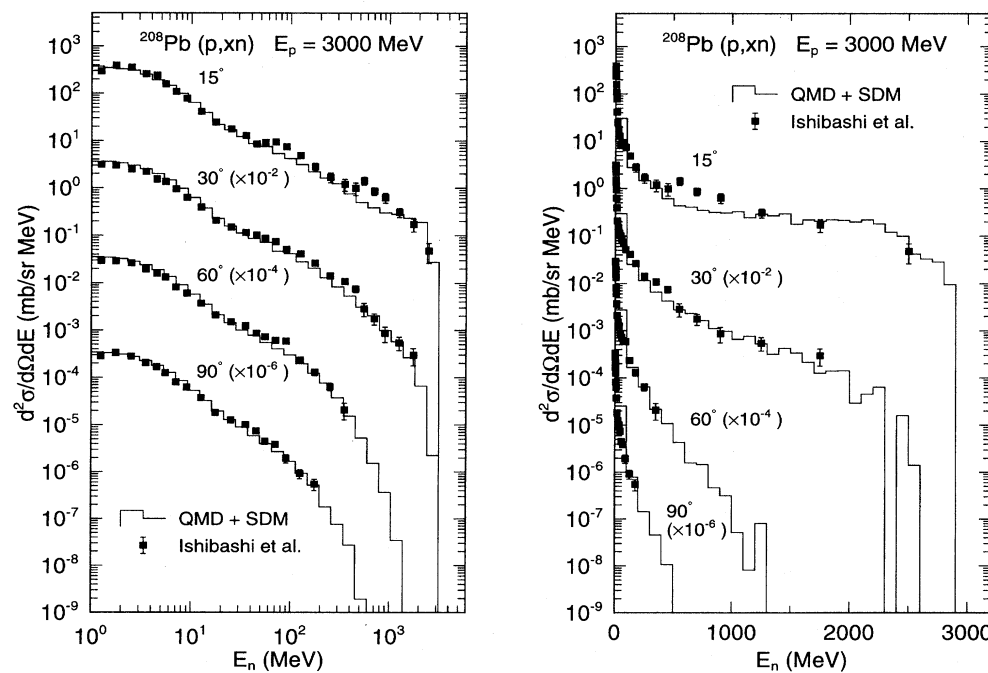
FIG. 15. Same as Fig. 14 for the reaction p (3000 MeV) $+ ^{208}$Pb.

the soft nucleon-nucleon interaction in Eq. (5) are taken common to all reactions and determined from the nuclear saturation condition. In addition, the final results are not so sensitive to them.

The first analysis of (p,xn) reactions by the QMD approach in the energy regime up to 800 MeV has been done by Peilert *et al.* [5]. The neutron spectra of their results are very similar to those of the present work above several tens of MeV. Their analysis, however, cannot predict the whole spectra of neutrons, since the contribution of the statistical decay from the excited fragments produced in the QMD calculation was not considered in their work.

Though the present results show overall agreement with the data for a very broad energy regime, one can see a systematic deviation from the data in the high energy part of the neutron spectra at the most forward angle at incident energy from 113 MeV up to 800 MeV (see the right-hand side of Figs. 10–13). We suppose that the soft nucleon-nucleon interaction is responsible for this deviation. One possibility is a momentum-dependent interaction that is not included in the present QMD, by which the nucleon could be affected coherently by the surrounding nucleons when its momentum is drastically changed by the hard nucleon-nucleon scattering. For the higher incident energies (see Figs. 14 and 15), this deviation disappears. In those cases, we have checked that the neutrons in the high energy part of the forward angle emerge after at least once experiencing the resonances of the nucleon, and that the effect of the soft interaction is relatively small. An analysis by the QMD including the momentum dependent interaction will be reported in a forthcoming paper.

IV. SUMMARY AND CONCLUSION

We have proposed quantum molecular dynamics (QMD) incorporated with the statistical decay model (SDM), aiming to describe various nuclear reactions in a unified way, and applied this model to the (N,xN') reactions. We have checked and found that the final results do not depend on the switching time when the QMD simulation is stopped and switched to the SDM calculation as long as the switching time is chosen between 100 fm/c and 150 fm/c for nucleon-induced reactions. Therefore little ambiguity is left with respect to the switching of the two different kinds of models to describe the whole process of the reactions in a unified way.

In order to describe the reactions at high incident energies up to 3 GeV, we have taken into account two baryonic resonances, for the $\Delta(1232)$ and the $N^*(1440)$ as well as the pions in the QMD model. The elementary cross sections related to these resonances and pions are basically taken from the experimental data. The angular distributions of the resonances, for which information is very poor in the experimental data, have been fixed to fit the $^{27}Al(p,p')$ data [25] at 3.17 GeV. It should be noted that the energy spectra of the nucleons from (N,xN') reactions on a small target are suitable quantities to obtain detailed information of the angular distribution of the resonances, while the pion spectra are useful to extract information on the mass distribution of the resonances.

In addition to the relativistic kinematics and approximately covariant prescription of the collision term, we have introduced Lorentz-scalar quantities to the arguments of the interactions and to the phase space factor. By these relativistic corrections together with the Lorentz contraction of the initial phase space distribution, the main part of the relativistic dynamical effects is approximately described in our QMD for the energy regime up to 3 GeV/nucleon. The validity of this model has been confirmed by analysis of the transverse flow for the heavy-ion collisions in comparison with the results obtained by the covariant version of quantum molecular dynamics (RQMD).

We have applied systematically QMD + SDM to the (N,xN') reactions for a broad range of incident energies from 100 MeV to 3 GeV and of target masses. The present model reproduced the overall features of the outgoing neutrons quite well without assuming any reaction mechanism, and without changing the parameter set. Although there are a lot of parameters in the model which have not been investigated extensively in this paper, the final neutron spectra analyzed here do not depend very much on them, for example, the equation of state (choice of the interaction), the width of the Gaussian wave packets, and the details of the statistical decay process. The main ingredients of the model, which produces the present results of the neutron spectra down to an energy of several MeV, are the parametrization of the elastic and inelastic elementary cross sections and the many-body dynamics itself, which have both been discussed in detail in this paper. We thus conclude that the present QMD + SDM scheme gives a unified picture of the three major reaction mechanisms of (N,xN') reactions; i.e., compound, preequilibrium, and spallation processes.

Finally, we should mention that the present model is ready to be applied directly to heavy-ion reactions in its original form. A study of heavy-ion reactions using this model is now under consideration.

[1] G. F. Bertsch and S. Das Gupta, Phys. Rep. **160**, 189 (1988), and references therein.

[2] J. Aichelin, Phys. Rep. **202**, 233 (1991), and references therein.

[3] Y. Yariv and Z. Fraenkel, Phys. Rev. C **20**, 2227 (1979); **24**, 488 (1981); K. K. Gudima and V. D. Toneev, Yad. Fiz. **27**, 67 (1978) [Sov. J. Nucl. Phys. **27**, 351 (1978)]; K. K. Gudima, H. Iwe, and V. D. Toneev, J. Phys. G **5**, 229 (1979).

[4] J. Cugnon, T. Mizutani, and J. Vandermeulen, Nucl. Phys. **A352**, 505 (1981); J. Cugnon, Phys. Rev. C **22**, 1885 (1980).

[5] G. Peilert, J. Konopka, H. Stöcker, W. Greiner, M. Blann, and M. G. Mustafa, Phys. Rev. C **46**, 1457 (1992).

[6] T. Maruyama, A. Ono, A. Ohnishi, and H. Horiuchi, Prog. Theor. Phys. **87**, 1367 (1992).

[7] T. C. Sangster *et al.*, Phys. Rev. C **46**, 1409 (1992).

[8] S. R. Souza, L. de Paula, S. Leray, J. Nemeth, C. Ngô, and H. Ngô, Nucl. Phys. **A571**, 159 (1994).

[9] Gy. Wolf, G. Batko, W. Cassing, U. Mosel, K. Niita, and M. Schäfer, Nucl. Phys. **A517**, 615 (1990).

[10] Gy. Wolf, W. Cassing, and U. Mosel, Nucl. Phys. **A552**, 549 (1993).

[11] Particle Data Group, J. J. Hernández *et al.*, Phys. Lett. B **239**, 1 (1990).

[12] *Total Cross Sections for Reactions of High Energy Particles*, edited by K.-H. Hellwege and O. Madelung, Landolt-Börnstein, New Series, Group I, Vol. 12, Pt. a (Springer-Verlag, Berlin, 1988).

[13] B. J. VerWest and R. A. Arndt, Phys. Rev. C **25**, 1979 (1982).

[14] J. H. Koch, E. J. Moniz, and N. Ohtsuka, Ann. Phys. (N.Y.) **154**, 99 (1984).

[15] F. Shimizu, H. Koiso, Y. Kubota, F. Sai, S. Sakamoto, and S. S. Yamamoto, Nucl. Phys. **A389**, 445 (1982).

[16] H. Sorge, H. Stöcker, and W. Greiner, Ann. Phys. (N.Y.) **192**, 266 (1989).

[17] E. Lehmann, R. K. Puri, A. Faessler, T. Maruyama, G. Q. Li, N. Ohtsuka, S. W. Huang, D. T. Khoa, and M. A. Matin, Prog. Part. Nucl. Phys. **30**, 219 (1993).

[18] T. Maruyama, S. W. Huang, N. Ohtsuka, G. Q. Li, and A. Faessler, Nucl. Phys. **A534**, 720 (1991).

[19] T. Maruyama, G. Q. Li, and A. Faessler, Phys. Lett. B **268**, 161 (1991).

[20] A. Bohr and B. R. Mottelson, *Nuclear Structure* (W. A. Ben-jamin, New York, 1969), Vol. 1.

[21] K. Niita, W. Casing, and U. Mosel, Nucl. Phys. **A504**, 391 (1989).

[22] A. Ohnishi and J. Randrup, Nucl. Phys. **A565**, 474 (1993).

[23] R. J. Charity *et al.*, Nucl. Phys. **A483**, 371 (1988).

[24] K. Ishibashi *et al.*, J. Nucl. Sci. Technol. **32**, 827 (1995); and private communication.

[25] H. En'yo *et al.*, Phys. Lett. **159B**, 1 (1985).

[26] W. B. Amian, B. C. Byrd, C. A. Goulding, M. M. Meier, G. L. Morgan, C. E. Moss, and D. A. Clark, Nucl. Sci. Eng. **112**, 78 (1992); and private communication.

[27] T. Nishida *et al.*, Report No. JAERI-M 86-116, 1986; and private communication.

[28] W. A. Coleman and T. W. Armstrong, Nucl. Sci. Eng. **43**, 353 (1971).

[29] T. W. Armstrong and K. C. Chandler, Nucl. Sci. Eng. **49**, 110 (1972).

[30] M. Blann, W. Scobel, and E. Plechaty, Phys. Rev. C **30**, 1493 (1984).

[31] M. Trabandt, W. Scobel, M. Blann, B. A. Pohl, R. C. Byrd, C. C. Foster, S. M. Grimes, and R. Bonetti, Phys. Rev. C **39**, 452 (1989).

[32] W. Scobel, M. Trabandt, M. Blann, B. A. Pohl, B. R. Reming-ton, R. C. Byrd, C. C. Foster, R. Bonetti, C. Chiesa, and S. M. Grimes, Phys. Rev. C **41**, 2010 (1990).

[33] H. Feshbach, A. Kerman, and S. E. Koonin, Ann. Phys. (N.Y.) **125**, 429 (1980).